Tectonophysics 786 (2020) 228461

Contents lists available at ScienceDirect

Tectonophysics

journal homepage: www.elsevier.com/locate/tecto

Predicting the propagation and interaction of frontal accretionary thrust faults with work optimization

Jessica McBeck[a,*], Michele Cooke[b], Laura Fattaruso[b]

[a] Physics of Geological Processes, The Njord Centre, Department of Geosciences, University of Oslo, Norway
[b] Department of Geosciences, University of Massachusetts Amherst, MA, USA

ARTICLE INFO

Keywords:
Accretionary prisms
Numerical simulations
Thrust fault growth
Work optimization

ABSTRACT

This study uses work optimization to predict the spatial and temporal development of faults. We focus on the growth of small fractures that develop into thrust faults at the toe of accretionary prisms because observations from physical laboratory accretion experiments provide rich data with which to validate the models, and the processes of accretionary thrust fault initiation remain unclear. In order to model these systems, we apply new implementations to the fault growth code GROW that improve its prediction of fault interaction using work optimization, including: 1) CPU parallelization, 2) a new growth algorithm that propagates only the most efficient fault in each growth increment, the *single* run mode, and 3) a new growth algorithm that only considers fault propagation from fault tips that host high sums of modes I and II stress intensity factors, K_G, the *limiting* mode. The new *single* and *limiting* mode produce the geometries that best match the observed geometries, rather than the algorithm that allows all the faults to propagate simultaneously, regardless of K_G, the *multiple* and *non-limiting* mode. The *single limiting* models predict that frontal accretionary thrusts initiate at the midpack or shallower depths, consistent with findings of previous studies. The thrusts propagate upward, link with the surface, and then propagate downward and link with the detachment. The backthrust tends to propagate before the forethrust, and then influences the forethrust propagation. This temporal and spatial sequence of faulting arises from the lower compression, higher shear strain, higher Coulomb stress and higher strain energy density that develop near the wedge surface and the inflection of the wedge slope. The models reveal that the final slip distributions do not reliably indicate the initiation location of the faults, in contrast to widespread assumptions.

1. Introduction

Faults develop through the propagation of individual fractures that may merge and link with each other (e.g., Reches and Lockner, 1994). Although empirical failure criteria provide valuable estimates on the critical loading required for fault development, they do not reveal the details of fault initiation and linkage, which requires the explicit consideration of multiple propagating fractures (e.g., Tang et al., 2001). Work optimization is a powerful method of predicting fracture development (e.g., Hardy et al., 1998; Masek and Duncan, 1998; McBeck et al., 2016, 2017a, 2017b; Madden et al., 2017). In this framework, each fracture propagates in order to optimize the mechanical efficiency of the system, as measured by the work done on the system.

Here, we propagate faults using work optimization within accretionary prisms because many aspects of fault initiation and development within the frontal zone of accretionary prisms remain unclear. In particular, the initiation depth of faults at the toe of accretionary prisms, and the temporal evolution of these faults, are poorly constrained. Accretionary thrusts may initiate near the detachment and propagate upward to the surface, or at shallower depths and propagate bilaterally, or near the surface and propagate downward to the detachment. Moreover, the frontal zones of accretionary prisms are ideal tectonic systems in which to study fault development because they are one of the few environments in which new faults propagate, rather than preexisting faults accommodating deformation. In addition, quantitative monitoring of physical analog accretionary wedges provides fine temporal and spatial resolution of thrust fault development in accretionary wedges (e.g., Dotare et al., 2016) to which we may precisely compare the numerical predictions.

With the work optimization approach implemented in the code GROW (McBeck et al., 2016), we may visualize the fine-scale temporal evolution of propagating and interacting faults. Here, we simulate fault development in GROW numerical models based on physical accretion experiments. Scaled laboratory accretion experiments provide rich data

* Corresponding author.
E-mail address: j.a.mcbeck@geo.uio.no (J. McBeck).

https://doi.org/10.1016/j.tecto.2020.228461
Received 15 January 2020; Received in revised form 23 April 2020; Accepted 26 April 2020
Available online 05 May 2020
0040-1951/

with which we can validate numerical models, in particular, when the numerical models are designed to match laboratory conditions (e.g., Buiter et al., 2016). Here, we follow this validation technique to assess the work optimization approach, and test the competing concepts of thrust fault development in accretionary prisms. We systematically vary the initiation depth of fractures at the toe of the prism, and then compare the modeled thrust fault geometry to the observed in order to constrain the initiation depth. This investigation of the growth of multiple fractures benefits from new, more computationally-efficient propagation algorithms that allow different rates of fault growth than used previously (e.g., McBeck et al., 2016, 2017b; Madden et al., 2017). We test these new fault growth algorithms implemented in GROW that model different degrees of synchronicity of fault growth and thus facilitate the simulation of many propagating fractures. This contribution thus presents new implementations to the code GROW, and then applies this new code in order to better understand fault growth at the toe of accretionary prisms.

2. Frontal thrust fault development in accretionary prisms

The processes that govern the initiation and timing of fault growth within accretionary prisms remain poorly constrained. In particular, the depth at which thrust faults initiate at the front of prisms is difficult to decipher from geophysical data. In the Hikurangi accretionary wedge, protothrusts imaged with high-resolution seismic reflection data intersect the seafloor, but do not appear to extend to the detachment (Barnes et al., 2018). The most outboard thrust in this wedge has maximum displacements closer to the detachment, perhaps suggesting initiation near the detachment. Alternatively, the thrust could have propagated downwards to the detachment and then developed greater slip near the intersection after the faults linked. In the Cascadia accretionary wedge, seismic reflection profiles suggest that some of the accretionary thrusts branch upward from a mid-level detachment, but terminate before reaching the surface (Adam et al., 2004). However, this apparent termination may arise from the loss of the visibility of structures in seismic imaging as they become more vertical. The precise details of early thrust fault development in accretion prisms, such as initiation location and hence the directionality of propagation, remain difficult to interpret from geophysical data.

In physical experiments, periodic photo acquisition records snapshots of the process of fault localization and provides a time series across a longer span of fault evolution than that generally provided by geophysical data of crustal accretionary prisms. Incremental strain fields of accretion experiments captured each 0.2 mm of shortening indicate that accretionary thrust faults develop from a diffuse region of elevated horizontal and vertical normal strains that collapse into subplanar volumes (McBeck et al., 2018). Extremely fine temporal resolution observations at 27 μm shortening increments identify series of transient, diffuse shear bands that migrate through the volume where the through-going thrust fault later develops (Dotare et al., 2016).

Some analyses have used the location of the highest shear strain along nascent thrust faults to identify their initiation depth. For example, shear strain fields captured in accretion experiments show that maxima in shear strain of the forethrust ramp localize in the midpack (Fig. 8 *E*-H in Marshak et al., 2019). This distribution may suggest that new forethrusts develop within the midpack and then propagate both upward and downward, rather than initiating at the basal detachment and propagating upward (Marshak et al., 2019). However, at earlier stages of this experiment, the shear strain fields host maxima both at the model base and in the midpack (Fig. 8C in Marshak et al., 2019), and similar magnitudes of shear strain along the forethrust ramp from the basal detachment to the midpack (Fig. 8D in Marshak et al., 2019). Although the forethrust hosts maximum shear strain in the midpack at later stages of development, the distribution of shear strain at earlier stages does not indicate an unequivocal nucleation location. Similar to interpreting the location of maximum slip as the fault nucleation region in geophysical data (e.g., Barnes et al., 2018), interpreting the maximum shear strain as indicative of initiation in laboratory experiments (e.g., Marshak et al., 2019) may lead to ambiguous or incorrect conclusions.

Such quantitatively monitored physical accretion experiments provide rich detail about the transition from diffuse compaction to strain localization and, in particular, constrain the horizontal position of thrust fault initiation. The photographic techniques employed in these experiments abut the temporal resolution limit imposed by motor speeds and photo acquisition rate. However, these techniques have not definitively constrained the vertical position at which thrust faults initiate within the sandpack.

3. Predicting fault development with work optimization

The work optimization framework proposes that fault networks develop to accommodate deformation that optimizes the total system efficiency, as quantified with metrics of the overall mechanical efficiency of the fault system (e.g., Hardy et al., 1998; Masek and Duncan, 1998; Dempsey et al., 2012; Cooke and Madden, 2014; Yagupsky et al., 2014; Olive and Behn, 2014). Work optimization is a global approach that incorporates the energetics of each fault in a network, as well as off-fault deformation of the host rock. When predicting fault propagation, this approach does not rely on local stress or strain distributions near growing fault tips, but instead calculates the work of the total system produced by different potential propagation paths. Work optimization considers the impact of both opening mode and shear failure on overall efficiency (e.g., Madden et al., 2017).

Here, we use work optimization to predict the development of growing and coalescing fractures in scaled experimental accretionary prisms using the fault growth code GROW (McBeck et al., 2016). Assessing the spatial development of fault networks with GROW provides predictions consistent with crustal segmented fault networks (McBeck et al., 2016, 2017b), planar accretionary thrust faults observed in laboratory experiments (McBeck et al., 2017a), and the linkage of laboratory faults under uniaxial and biaxial conditions (Madden et al., 2017).

GROW propagates faults in the direction that optimizes the total external work, W_{ext}, acting on the deforming system, i.e., the total system efficiency. GROW simulates fault propagation and interaction by adding small sections of new fault (i.e., elements) at each model time increment in the direction that optimize W_{ext}. Each increment of fault growth thus defines the model time increment, and the rate of fault growth thus arises from the length of added elements. This implementation thereby provides precise histories of the spatial and relative temporal evolution of faulting that are not yet available from crustal or experimental observations. Comparing the numerical fault geometries produced by GROW to observed experimental fault geometries enables assessing if work optimization can predict the fine-scale evolution of thrust fault development. Previous GROW implementations only allowed assessing the accuracy of the fault geometries (e.g., McBeck et al., 2016; Madden et al., 2017). Our new implementations also enable assessing the accuracy of the relative timing and rate of fault propagation. To investigate temporal questions about the evolution of the linkage and coalescence of faults from seed fractures, we test growth algorithms that 1) only grow the most efficient fault at each time increment, 2) only assess fault growth from fault tips with high mode-I and mode-II stress intensity factors, and 3) propagate all the growing fault tips simultaneously in each increment.

4. Methods

We propagate faults using a revised version of GROW and so describe the new implementations to the code. To validate the implementations, we compare the results to well-documented measurements of shear strain in accretion experiments performed at the

University of Cergy Pointoise (UCP). The details of these experiments are presented in full in McBeck et al. (2018).

4.1. GROW

Following the initial implementation of GROW (McBeck et al., 2016), we incorporate several new functionalities that reduce the run time and improve the ability to test several fault growth algorithms. Here, we describe the functionality of the original code, which McBeck et al. (2016) describes in full.

GROW is a script that wraps around the 2D plane strain linear elastic boundary element method tool Fric2D (Cooke and Pollard, 1997). GROW uses Fric2D to calculate the shear and normal tractions and displacements along boundaries and growing fractures in models with varying (growing) fracture geometries, and hence the total external work of the system, W_{ext} (Eq. (1)). GROW propagates fracture networks by selecting the most work efficient direction of fracture propagation from the fracture tip using W_{ext}. The total external work is the area under the force-displacement curve from the onset of loading to the particular stage of interest. The external work of the system may be calculated from dot product of the tractions, $\vec{\sigma}$, and displacements, $\vec{u}$, integrated along the boundaries of the system, B, and integrated over the loading steps, L, as

$$W_{ext} = \int_1^L \oint_B \vec{\sigma} \cdot \vec{u} \; dB \; dL \tag{1}$$

In the models, L determines the number of steps over which the applied load is increased linearly to the target load. When displacements are applied, L thus controls the magnitude of displacement applied to the model for each loading step, and Eq. (1) then integrates over the history of the applied displacement. The sign conventions of the displacements and tractions are defined relative to the element orientation, following the conventions of Fric2D (e.g., Cooke and Pollard, 1997).

When displacements are applied to the boundaries, the most efficient fault systems will have the lowest W_{ext} because efficient systems require lesser loads to accommodate the applied displacements. Under traction loading, the most efficient fault systems will be those with greatest W_{ext} due to the greater resulting displacement. With displacement loading conditions, as employed here, the most efficient systems produce the greatest negative ΔW_{ext}, which is the change in external work produced by an increment of fault growth.

The user prescribes the angle range over which GROW searches for the most efficient orientation of growth from each fracture. This angle is measured relative to the fracture tip. A typical angle range may be 90° to 270°. The user also prescribes the resolution of the search, with typical values of 10°. With these parameters, for each growing fault GROW searches for the most efficient direction of fault growth at 90°, 100°, 110°, …, 260°, 270° from that fault tip. After GROW identifies the most efficient orientation with the prescribed search resolution, the second tuning step of GROW searches with a higher resolution for the most efficient orientation at half the initial search resolution. So, if the most efficient orientation found is 180° for the parameters used above, GROW then identifies the most efficient system of models with new fracture elements oriented at 175°, 180° and 185°. When multiple fault tips are growing, then the tuning step assesses the efficiency of fault geometries that include all of the combinations of orientations at half the initial search angle resolution at each growing fault tip (McBeck et al., 2016).

4.2. New GROW implementations

Here, we describe the new implementations to the code, including parallelization and varying methods of fault propagation.

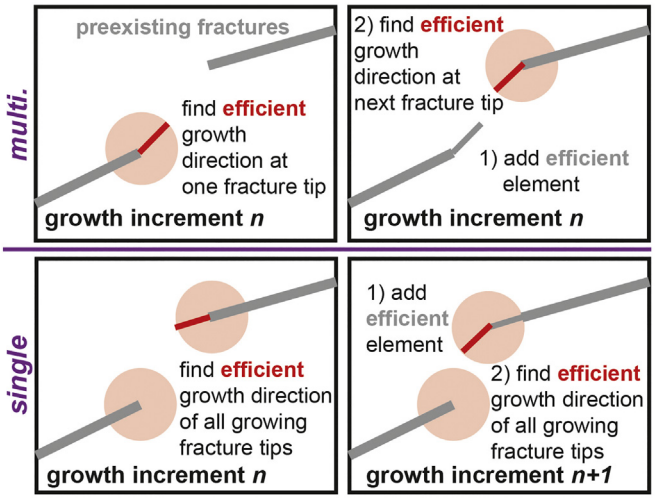

Fig. 1. Schematic of alternative fault growth algorithms implemented in this study: *multiple* run mode (top), and *single* run mode (bottom). In the *multiple* mode, each fracture tip grows an element along the most efficient orientation in each growth (time) increment. Fractures grow in alphanumerical order by the names such that the most efficient growth direction from one fracture tip is found (left panel), that element is added, and then the most efficient growth direction is identified and added at the next fracture tip (right panel). These additions occur in one growth increment. In the *single* run mode, only the most efficient fracture tip grows in each increment. First, the gains in efficiency produced by the individual growth of the fracture tips are calculated, and the most efficient growth direction is identified (left panel), and then that one element is added, and the gains in efficiency from all fracture tips are calculated again (right panel). Growth shown in the left panel occurs in one increment, and growth shown in the right panel occurs in the next increment.

4.2.1. Parallelization

In order to shorten the run time, we parallelized GROW so that the code may run on any number of processors simultaneously. This parallelization allows multiple processors to simultaneously solve for the deformation associated with different potential fracture propagation paths. The amount that parallelization reduces the run time depends on the number of growing fracture tips and the resolution of the search for the most efficient growth direction. For example, with four growing fracture tips and 18 potential propagation paths (i.e., searching between 90° and 270° from the fracture tip in increments of 10°) 72 boundary element method model runs of the code Fric2D are required to determine the four potential directions of fault growth from each tip, for just one growth increment. In this case, the new parallelization implementation would reduce the run time of one growth increment by a factor of up to 72, if 72 cores are available on the system.

4.2.2. Alternative growth run modes

With the resulting improved run time, we implemented two new methods of growing multiple fracture tips (Fig. 1). In the original growth algorithm (*multiple* run mode), the tip of each fracture propagates in each growth increment if that tip fails in either tension or shear. Fractures propagate via the addition of new elements at their tip. In the new growth algorithm (*single* run mode), only the fracture tip that produces the greatest increase in efficiency, $|\Delta W_{ext}|$, of the system grows in each growth increment. If one tip produces much greater $|\Delta W_{ext}|$ than all other tips, then it might propagate for multiple increments. Thus, the rate of propagation depends on the gain in efficiency produced by fracture propagation, and the element length. Consequently, the *single* run mode uses work optimization to predict the relative timing of growth among fracture tips, as well as the geometry of new fracture growth. In contrast, the *multiple* run mode uses work optimization to predict the geometry, but does not use efficiency to determine the relative timing of fracture growth. By comparing the results

of these two growth modes to experimental observations, we assess the reliability of using efficiency criteria to predict the fine-scale spatial and temporal evolution of fault growth.

In order to better investigate the simultaneity of fault growth, we implement an option that limits the assessment of propagation only to those fracture tips with high mode-I, K_I, and mode-II, K_{II}, stress intensity factors. We refer to this option as *limiting*, and not using this option as *non-limiting*. The *limiting* option exploits the likelihood that propagation from fracture tips with the highest K_I and/or K_{II} leads to the largest gains in efficiency. We identify the maximum of the sum of K_I and the absolute value of K_{II}, K_G, among all the fracture tips, where.

$$K_G = K_I + |K_{II}| \quad (2)$$

The absolute value of K_{II} ensures that left- and right-lateral slipping fractures are considered equally. Then, we assess fault growth at each prescribed orientation among only the fracture tips with K_G greater than 90% of the maximum K_G. The *limiting* option saves CPU time by not assessing fractures with relatively low K_G. Either run mode (*single* or *multiple*) may use the *limiting* option. In the *single* run mode, GROW identifies the one potential growth orientation that produces the largest gain in efficiency, and grows this fracture tip. In the *multiple* run mode, GROW propagates all of the fracture tips that host high K_G by searching for, and propagating the most efficient growth direction at each fault tip one-by-one (Fig. 1).

4.3. Experimental data for model validation

In this study, we propagate faults in numerical models that simulate quantitatively-monitored dry sand accretion experiments performed at the University of Cergy-Pontoise (UCP). McBeck et al. (2018) describes the setup of these experiments, and so here we briefly describe the experimental data used to validate the numerical models. The deformation apparatus at UCP was carefully designed and prepared to mitigate the effects of side wall friction, which impact the fault geometry observed through the glass side walls. The four experiments used here include two suites of experiments that either include or exclude a basal layer of glass beads, and two suites of experiments with opposing apparatus configurations, in order to mitigate side wall friction effects. In the experiments with opposing configurations, horizontal contraction is applied either via movement of the vertical backwall that slides over a base, or via movement of the base under the stationary backwall. Photos of the sandpack cross sections through both glass side walls of the 1 m × 1 m sandbox at UCP provide detailed incremental displacement fields via digital image correlation. The incremental shear strain fields calculated from the incremental displacement fields reveal localized slip along the detachment and thrust faults. Despite the differences in the experimental set ups, the geometries of the first thrust fault pair recognized from the strain fields, including the position and dip of the thrusts, are similar in all four experiments (Fig. S1).

The precise position and dip of the observed faults differ typically by 1–3 cm from the backwall and 5–10°, respectively, for each thrust fault geometry observed through the two glass sidewalls of the four experiments. Consequently, we define a zone of observed thrust faulting (gray in Fig. S1) to which we compare the numerically-predicted fault geometries.

The geometry of the first thrust fault pair in these experiments also resemble those of many other accretion experiments in dry sand (e.g., Schreurs et al., 2016). The accretion benchmarking study of Schreurs et al. (2016) with different types of sand, similar boundary conditions, and performed in 16 different labs show that the geometries of the first thrust fault pair that develop are similar to those in these experiments. The dip and position of the thrusts outlined with the gray zone in the subsequent figures here match the geometry of the first thrust faults that develop in the experiments of McBeck et al. (2018), as well as the accretion experiments within the benchmarking analysis of analog wedges of Schreurs et al. (2016).

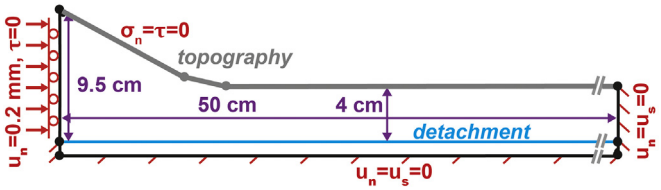

Fig. 2. Numerical model setup designed to produce deformation observed in physical accretion experiments. The base and right sides of the model are held fixed with no normal or shear displacements. A constant normal rightward displacement (0.2 mm) is applied to the vertical backwall with no shear tractions, allowing the wall to displace vertically as the model thickens upon shortening. The top boundary of the wedge may deform under no normal or shear tractions. The detachment fault (blue) spans the length of the 50 cm long model. The model topography and thickness match the dimensions of physical experiments performed at UCP (McBeck et al., 2018), and many other previous experiments (e.g., Schreurs et al., 2016). (For interpretation of the references to colour in this figure legend, the reader is referred to the web version of this article.)

4.4. Numerical model geometry and loading

We design the numerical model geometry so that it matches the overall geometry of the cross section of the experimental wedges described in McBeck et al. (2018) (Fig. 2). Our previous modeling of accretionary systems predicted the geometry of planar thrust faults that cross the entire sandpack, and that developed in accretion experiments that were smaller in scale (McBeck et al., 2017a) than the present experiments. The new models that simulate the new and larger experimental apparatus include a frictional sliding fault that extends across the 50 cm length of the model, and represents the basal detachment fault. Whereas the previous models of McBeck et al. (2017a) had displacement basal boundary conditions to represent detachment slip, the models of this study allow the detachment to frictionally slip in response to loading of the system. This fault is located 0.5 cm above the base of the model, which is held fixed with no shear or normal displacements. To simulate horizontal contraction, we initially apply 0.2 mm of horizontal, rightward displacement to the left backwall. This magnitude matches the magnitude of backwall displacement observed in digital image correlation in successive increments of the experimental wedges. We allow this wall to move upward and downward with no shear tractions in order to simulate the observed thickening of the sandpack at the backwall. The vertical wall at the right is held fixed. The upper surface is allowed to displace with no normal or shear tractions. These loading conditions cause the total external work of the system to arise only from the change in the normal force acting on the left backwall (Eq. (1)).

The geometry of the upper surface simulates the initial topography of the physical sand wedge. This topography includes a wedge of sand adjacent to the backwall and a flat sandpack outboard of this wedge. This wedge helps ensure that the first thrust fault pair does not develop immediately adjacent to the backwall, but instead initiates near the toe of the initial wedge (e.g., Schreurs et al., 2016).

In each Fric2D input file we apply 0.2 mm of rightward backwall displacement, u_n, in the first loading step (e.g., in Eq. (1) $L = 1$). Because some of the preexisting faults do not propagate under this displacement, and others only propagate for a few model growth increments, we follow the first loading step with several additional loading steps. Each subsequent loading step adds 0.2 mm of backwall displacement until the faults link with each other or the boundaries of the system. One loading step, where the backwall displacement is displaced an additional 0.2 mm, may include several fault growth increments, or no growth increments, if none of the potential fault elements added to faults fail either in tension or Coulomb shear failure.

Many of the intact sand material properties and fault properties used in these models (Table S1) are well-characterized, including the

Poisson's ratio (0.2), and the effective friction of faults that develop within sand (0.4–0.6), and the basal detachment between the sandpack and the glass base of the experimental sandbox (0.3) (e.g., Gercek, 2007; Klinkmüller et al., 2016). Analysis of experimental data from the UCP sandpacks provide estimates of the effective Young's modulus preceding thrust fault development that range from 0.5–1 MPa, with averages of 1 MPa (McBeck et al., 2018).

In this study, we use GROW to gain insight on the location of thrust fault initiation by seeding models with initial small fractures geometries at differing locations, allowing GROW to propagate the potential faults, and assessing the similarity of the predicted fault paths to the faults observed in the physical experiments. We place two seed fractures within the observed fault zone, one for the backthrust and one for the forethrust, and allow both fracture tips to grow.

The seed fractures included in GROW cannot represent all of the many mechanical weaknesses present in dry sand accretionary wedges (i.e., the boundary between individual sand grains). Instead, the initial fractures represent an intermediate stage of strain localization or fracture coalescence at a scale larger than sand grain boundaries, but smaller than the system size, at about 10% of the wedge height for these models. Introducing the seed fractures with this method parameterizes the microscopic process of sand grain rotation and rearrangement that occurs along hundreds and thousands of sand grains in the experiment prior to fault localization. Consequently, we test fault growth and interaction in systems that include two initial zones of weakness.

The fractures are one element long (0.5 cm) and oriented along the observed thrust fault dip. We use the same range and resolution of angle search for each fracture, from 90°-270° clockwise from the fault tip in increments of 10°, with 5° resolution for the tuning step.

GROW enables assessing fault growth from a point, such that the dip of the initial fault does not have to be prescribed, but determined by work optimization. In these models, however, this method yields four highly efficient growth paths that correspond to the upward or downward growth of the backthrust or forethrust at each point (Fig. S2). While the orientations resemble the forethrusts and backthrusts that eventually develop, the similarity of efficiencies of these four orientations produces unreliable predictions of growth because GROW only predicts a single direction of growth from one fracture tip, and not multiple directions of growth from a tip. Consequently, we prescribe the orientation of the initial fractures as parallel to the observed thrusts.

5. Results

First, we discuss the stress and strain fields of the wedges preceding fault growth, and the corresponding difficulty of predicting potential fault initiation positions. Then, we describe the growth and interaction of faults from pairs of seed fractures at varying depths with the various fault growth run modes, and we assess the match of the model predictions to the experimental observations. Then, we describe the evolution of efficiency with fault propagation in this suite of nine models, and by linking differences in the observed and numerical fault geometries to the overall efficiency.

5.1. Predicting thrust fault initiation depth

To determine the location of thrust fault initiation, we use experimental observations of faulting to guide the lateral (horizontal) positions of the initial seed fractures from which faults grow. An alternative approach of selecting the fracture location could rely on the stress and strain fields of the numerical models prior to fault development. For example, the lowest compressive stress, highest shear stress, highest Coulomb stress, or highest strain energy density could identify potential locations of fault initiation (e.g., Baud et al., 2000, 2014; Olson and Cooke, 2005; Del Castello and Cooke, 2007; Weiss et al., 2018; Du and Aydin, 1993; Okubo and Schultz, 2005; Fattaruso et al., 2016).

To test the consistency of these approaches, we show the 2D fields of the first invariant of the stress tensor (indicative of mean normal stress), the magnitude of shear stress, the maximum Coulomb stress, and the strain energy density prior to the development of faults. Faults are expected to develop in regions with lower compressional stress (greater first invariant, indicating dilatancy associated with onset of shearing (e.g., Lohrmann et al., 2003)), higher magnitudes of shear stress, higher Coulomb stress, and higher strain energy density.

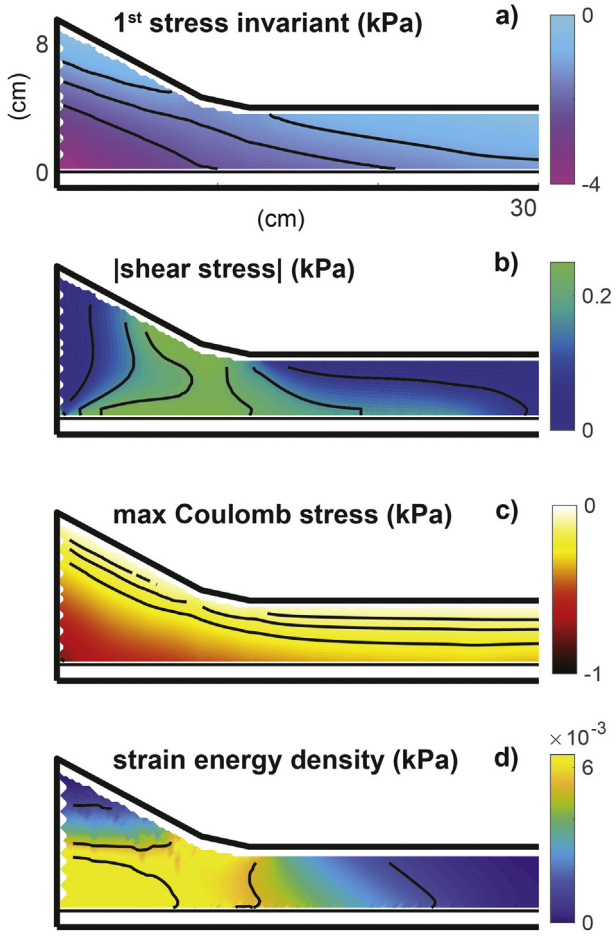

Fig. 3. Potential criteria to select fault initiation position: first invariant of the stress tensor, $\sigma_{xx} + \sigma_{yy}$, with compression < 0 (a), magnitude of shear stress, τ_{xy} (b), maximum Coulomb stress (c), and strain energy density, $\frac{1}{2}(\sigma_{xx}\varepsilon_{xx} + \sigma_{yy}\varepsilon_{yy} + 2\tau_{xy}\varepsilon_{xy})$ (d). Black contour lines show regions with values between the 50th, 75th and 90th percentile. These criteria do not yield precise predictions of potential fault initiation, but only broad areas that suggest different locations of initiation. The 1st stress invariant and Coulomb stress fields predict that faults will initiate in regions near the topography. In contrast, the shear stress and strain energy density fields predict that faults will initiate in the broad region from the corner of the wedge to the topography slope inflection point.

In these models, the zones with the lowest compressional stresses (least negative first invariant) and highest Coulomb shear stress occurs near the surface of the wedge, as expected from the gravitational loading conditions (Fig. 3). The zones with the largest shear stress and strain energy density span from the inflection of the wedge surface and the lower left corner of the model, adjacent to the backwall. These zones of high shear stress and strain energy density arise from both the loading applied to the left backwall and wedge slope inflection, which serves to localize shear stress.

Each of these fields do not reveal precise positions of potential fault initiation, but highlight broad areas within which faults could nucleate (Fig. 3). Moreover, the broad areas of potential fault initiation predict different initiation depths. In the models, the zone with the highest

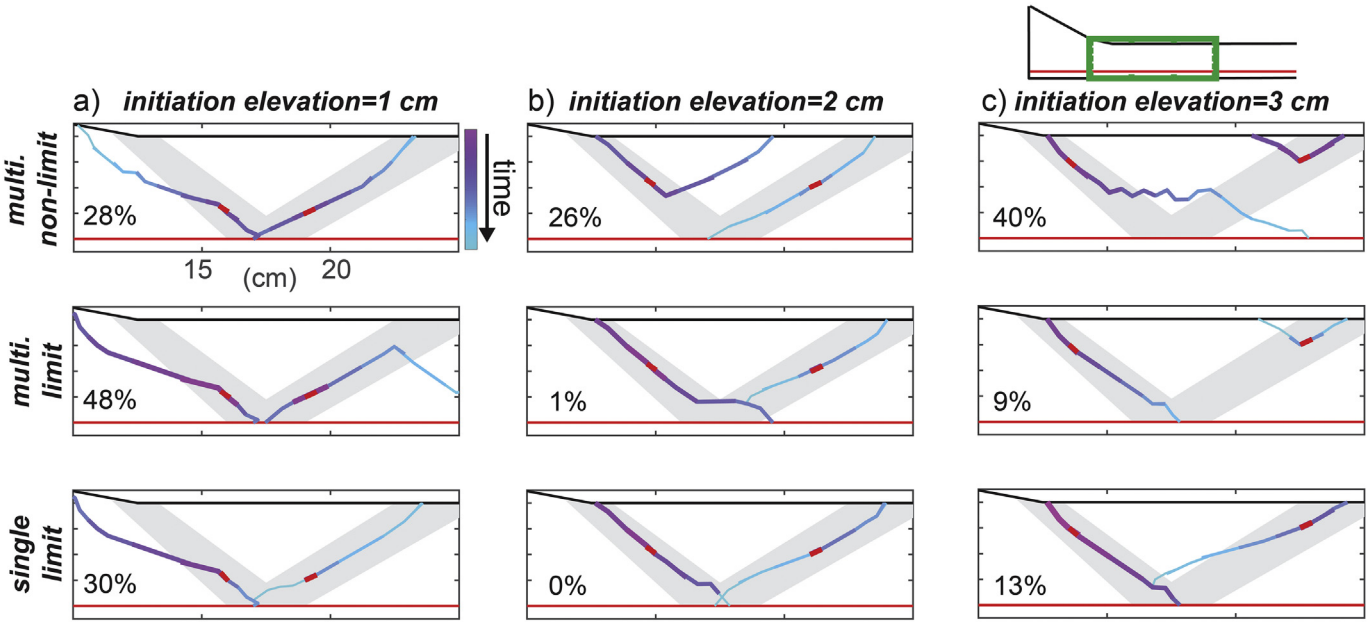

Fig. 4. Predicted fault growth for models with pre-existing fractures at 1 cm (a), 2 cm (b) and 3 cm (c) above the detachment, and three run modes: *multiple non-limiting* (top), *multiple limiting* (middle), and *single limiting* (bottom). See the method section 4.1.2 for details of differences between the run modes. Green box in the sketch at the top shows the region of the model shown in the rest of the figure. Fault segments are colored by the model growth increment when they grew. Horizontal red line indicates the basal detachment. Thicker red lines show the seed fractures from which the faults grew. Gray areas show the zone of faulting typically observed in many previous physical experiments. Percentages in lower left corners indicate the percent of fault length that lies outside the observed region. (For interpretation of the references to colour in this figure legend, the reader is referred to the web version of this article.)

compressional stress (most negative first stress invariant) overlaps the zone with the highest shear stress and strain energy density. This overlap leads to conflicting predictions of fault initiation location from these criteria because we expect fault development to occur in regions with lower compression and higher shear stress and strain energy density. Consequently, we use GROW to systematically test the depth of thrust fault initiation by seeding initial fractures at different depths. We note that the broad region of predicted fault initiation area outlined by the shear stress and strain energy density field includes the region in which backthrusts develop.

5.2. Sensitivity of fault development to growth algorithm

We compare the modeled fault geometries that nucleate at the same depth but propagate with different run modes. In the *multiple* run mode, we can either assess growth from all fault tips or use the *limiting* option that propagates fractures from only a few, or sometimes only one, fault tip that has K_G greater than 90% of the maximum K_G (Eq. (2)). By comparing the length of fault that strays outside the zone of faulting typically observed in many previous physical accretion experiments (e.g., Schreurs et al., 2016) (gray zones in Fig. 4), we assess the accuracy of the different growth run modes for capturing thrust fault growth at the front of accretionary prisms, and perhaps other tectonic environments. We note that seismic imaging of natural accretionary wedges (e.g., Booth-Rea et al., 2008) reveals thrust fault pairs with similar dips to the experimental geometries. So, the overlap of the numerical fault geometries with the gray region on Fig. 4 indicates the agreement of the numerical fault geometries to the geometries of faults in scaled physical dry sand experiments, and natural accretionary wedges.

When the faults grow in the *multiple non-limiting* run mode (Fig. 4), the placement of the initial fractures within the model influences the resulting fault development. In particular, the relative timing of when the fault tips intersect the detachment, and later when they intersect the surface, depends on the distance from the fractures to the detachment and the surface. This correlation of fracture depth and relative timing occurs in GROW because the rate of fault propagation depends on the length of fault propagated during a growth increment (i.e., model time increment), which is the element length multiplied by the number of fault tips growing. For example, when the seed fractures are located at 1 cm from the detachment, and propagate with the *multiple non-limiting* run mode, the fractures propagate bilaterally at the same rate, and so the new faults intersect the detachment before the surface (Fig. 4, Ani. S1). After intersecting the detachment, both the backthrust- and forethrust-verging fractures propagate upward and intersect the surface. The forethrust-verging fracture propagates completely within the zone of observed thrust faulting (gray in Fig. 4). However, the backthrust-verging fracture propagates outside of this zone for 50% of its length. Note, the percentages on Fig. 4 are the percentages of the modeled fault length that propagate outside the observed (gray) region of thrust fault development, providing a quantitative value of how well the models match the observed thrust fault geometries.

In order to compare the three run modes directly, we describe the fault growth evolution in models with the same seed fracture position, at 1 cm above the basal detachment (Fig. 4a). When the fractures are located at this depth, and propagate with the *multiple limiting* run mode, first, fault growth occurs at both tips of both fractures (dark purple segments in Fig. 4, Ani. S2). But then only the upper tip of the backthrust fracture has $K_G > 90\%$ of the maximum K_G, and so it propagates upward to the surface while no growth occurs from the other fault tips (purple segments in Fig. 4a). The intersection of this fault with the surface produces a large gain in efficiency relative to the other increments of growth (Ani. S2). After the fault intersects the surface, the lower tips of the backthrust and forethrust propagate downward, and link with the detachment. Then, the upper tip of the forethrust begins to propagate upward (blue segments in Fig. 4a). However, the forethrust does not reach the surface, but instead propagates non-linearly and toward the detachment, until linking with the detachment with an irregular geometry (outside the region shown in Fig. 4a). At the stage when the forethrust propagates non-linearly (Fig. S3a), the distribution of the gain of efficiency for different propagation directions shows that propagation of 220–260° from the tip produces only slightly higher

gains in efficiency than the expected colinear growth direction of 180° from the fault tip (Fig. S3). So, the fault had a similar likelihood of propagating at 40° from colinear as propagating along a colinear direction. In summary, using the *limiting* option with the *multiple* run mode changes the timing of fault development by only assessing tips with high K_G. In these models, employing the *limiting* option prevents the forethrust from propagating until later in simulation, after the backthrust develops.

When the fractures propagate at 1 cm above the detachment in the *single limiting* run mode, first the upper tip of the backthrust propagates and intersects the surface in a geometry similar to the geometries produced in the other run modes (purple fault segments Fig. 4a, Ani. S3). Then the lower tip of the backthrust propagates and meets the detachment. Next, the upper tip of the forethrust propagates and meets the surface. Then the lower tip of the forethrust propagates, and meets the detachment (blue fault segments in Fig. 4a). The linkage of the backthrust and forethrust with the surface produces larger gains in efficiency than the previous and following increments of growth (Ani. S3). The geometry of the backthrust remains similar in models using different run modes, despite the different synchronicity of fault propagation considered in the different run modes. This similarity occurs because the backthrust propagates before the forethrust, and so its geometry is less dependent on the run mode than the forethrust.

The *multiple limiting* and *single limiting* run modes produce fault geometries that best match the observed fault geometries when the faults initiate at 1 cm above the detachment. However, of the initiation depths tested, the 1 cm initiation depth produces the fault geometries that deviate the most from the observed geometries.

5.3. Sensitivity of fault development to initiation depth

Of the suite of nine models, with three initiation depths and three run modes (Fig. 4), the numerical geometries with faults that most closely match the typically observed thrust geometry include fault initiation from the mid-pack or shallower depth, and the run modes that restrict growth to fault tips that host high stress intensity factors. The original run mode of GROW (*multiple non-limiting*) produces the most irregular fault geometries of all the run modes, propagating 28–40% of their length outside the observed region of faulting (Fig. 4). The fault geometries that nearly completely overlap the observed thrust faulting zones include growth from the midpack (2 cm above the detachment) in the *multiple limiting* (1% outside the observed zone) and *single limiting* (0% outside) run modes. In each of these models, first the backthrust propagates upward, links with the surface, and then propagates downward and links with the detachment. When the backthrust finishes propagating, the forethrust then grows upward, links with the surface, and then grows downward and links with the detachment. The better match of the fault geometries for the mid-pack initiation depths suggest that accretionary thrust faults may initiate in regions of reduced normal compression and higher Coulomb stress (Fig. 3). The preference of backthrusts to develop before forethrusts may arise from the lower compression, higher shear stress, higher Coulomb stress, and higher strain energy density, which promote fault propagation in the region near the wedge surface slope inflection (Fig. 3).

5.4. Efficiency evolution

GROW propagates faults along the path that produces the greatest gains in efficiency and, depending on the growth run mode, in the order that produces the greatest gains. Here, we examine the evolution of system efficiency in the nine models of growth at different initiation depths and run modes (Fig. 5). With the displacement loading boundary conditions of these models, decreasing external work, W_{ext}, indicates gaining efficiency. Under displacement loading, lower W_{ext} indicates that lesser normal and shear tractions on the system boundaries are required to accommodate the applied displacement (Eq. 1). With the loading conditions of these models, only the backwall boundary contributes to W_{ext} because all of the other boundaries have either zero applied displacements or tractions. Consequently, changes in W_{ext} of these models correspond to changes in the normal tractions on the backwall.

The nine models require different numbers of applied loading steps, and thus magnitudes of backwall displacement both for the initiation of the fractures (u_n = 0.2–0.4 mm), and for the faults to intersect the boundaries or other faults, thus terminating the simulation (u_n = 0.4–0.6 mm). During each applied loading step, faults may propagate for many growth increments via the addition of new elements, until they no longer propagate under the applied displacement, or they intersect another fault or model boundary. Each fault growth increment may be considered to be the smallest increment of model time (i.e., growth time increment). The increase in applied displacement for each loading step produces a step-wise increase in backwall force and W_{ext}. So, we report the W_{ext} at each growth increment relative to the W_{ext} at the start of that loading step, ΔW_{ext}.

Models with different initiation depths require different applied backwall displacement, u_n, for the fractures to start growing. When the fractures initiate at 1 cm above the detachment, they require double the u_n (0.4 mm) to begin growing than when the fractures initiate at 2 cm or 3 cm (0.2 mm). This difference in loading suggests that if mid-level or shallow fractures are appropriately oriented for failure, they will fail before deeper fractures. This result is consistent with the closer agreement of the observed and predicted fault geometries that initiate at the mid-level or shallower, compared to the faults that initiate near the detachment.

The one model that requires only 0.2 mm of backwall displacement for the faults to link with each other or the model boundaries includes fractures initiating at 3 cm above the detachment and propagating under the *multiple limiting* run mode (green in Fig. 5c). This model may require only one loading step in part because lesser total fault length is propagated in this model than the others (Fig. 4). In general, the *multiple* run mode typically requires lower applied displacement than the other run modes because more total fault length is added during one growth increment in this mode than the others (e.g., Fig. 1) because all the fracture tips may grow in one increment. Consistent with the greater fault length propagated in one growth increment, the evolution of ΔW_{ext} demonstrates that the gain in efficiency is larger at each growth increment in the *multiple* run mode than the other modes.

The evolution of ΔW_{ext} also shows that when the fractures at 1 cm above the detachment begin to grow, they produce larger gains in efficiency in each growth increment than the fractures at shallower depths (Fig. 5). Correspondingly, when the fractures that initiate at 2 cm grow, they produce larger gains in efficiency than the fractures that initiate at 3 cm. This trend indicates that upward propagating faults have greater energetic gain than downward propagating faults. The greater slip along fault segments in the upper portion of the wedge relative to segments at deeper depths in many of the models (Figs. 6, 7) contributes to the greater energetic gain of upward fault growth relative to downward growth. This preference for upward propagation may arise because the faults are propagating into regions with the greatest potential for failure, with the highest Coulomb stress, and lowest compression (Fig. 3). The preference for the upward propagation of the backthrusts, in particular, is driven by the high strain energy density and high shear stress zone near the surface slope inflection.

Following the premise that experimental (and crustal) faults grow in the direction, and with the relative timing, that optimizes W_{ext}, we expect that the numerical fault geometries that best match the typically observed fault geometries will also be the most efficient. So, here we correlate the W_{ext} of models with the final propagated fault geometries, under 0.4 mm of applied displacement (Fig. 6). Under the applied displacement boundary conditions, lower W_{ext} indicates more efficient systems that host lower normal tractions acting on the backwall. In particular, we correlate the difference between the observed and

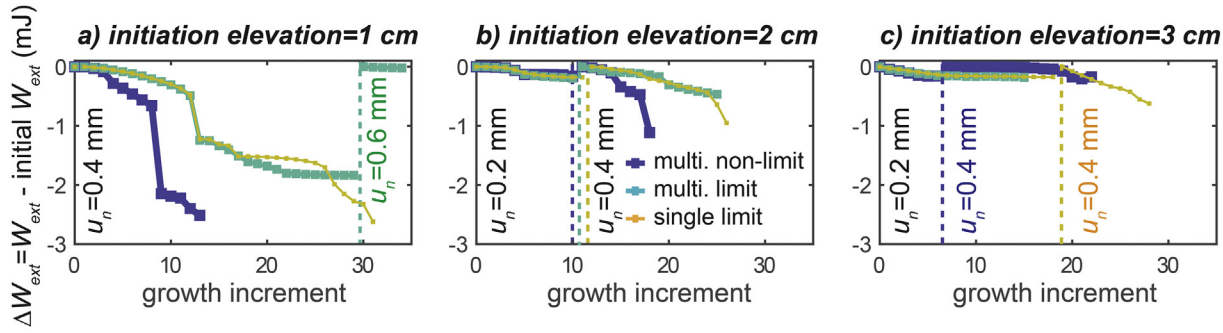

Fig. 5. Evolution of system efficiency throughout models with each run mode and seed fracture elevations of 1 cm (a), 2 cm (b) and 3 cm (c) above the basal detachment. System efficiency shown as the total external work, W_{ext}, acting on the system minus the W_{ext} at the growth increment when the backwall normal displacement, u_n, was last increased. Vertical dashed lines indicate when we increase u_n, after all of the faults in the model stop growing under the lower u_n of the previous loading step. Numbers near dashed lines indicate the new applied u_n. When faults initiate at 1 cm above the base, they produce the largest gains in efficiency, but require higher applied backwall displacement to begin propagating (0.4 mm).

modeled fault geometries to W_{ext} calculated from the percentage of thrust fault length that lies outside the observed zone of faulting, p, and from the mean tortuosity of the numerical thrust faults. The tortuosity of the numerical faults is the total (potentially curved) length of the fault, C, divided by the straight-line distance between the endpoints of the fault, L, C/L. Lower tortuosity indicates geometries more similar to the observed planar thrust geometry with $C/L = 1$.

In contrast to expectations, the models that most closely match the position of the observed geometry, with the lowest p, do not consume the lowest W_{ext} (Fig. 6a). These models do not produce a clear trend between p and W_{ext}, with only $R^2 = 0.02$ of a linear fit. However, there is a weak positive correlation between the tortuosity of the thrust faults and W_{ext}, with $R^2 = 0.21$ (Fig. 6b). This correlation arises because thrust fault tortuosity influences how much the thrust faults slip (Fig. 6c). More planar faults with lower tortuosity should slip more than faults with more complex geometries. The moderate-strong negative correlation of tortuosity and the total thrust fault slip ($R^2 = 0.57$) supports this expectation (Fig. 6c). We calculate the total thrust fault slip by summing the slip on each (equal-length) element of the thrust faults. The relationship between tortuosity and slip contributes to the strong negative correlation between W_{ext} and the total thrust fault slip, with $R^2 = 0.79$ (Fig. 6d).

Greater slip and lower tortuosity of the thrust faults produce more efficient systems with lower W_{ext}. The example fault geometries shown in Fig. 6e demonstrate that while two models may have similar p, they may have different tortuosity and slip distributions, which produce different W_{ext}. The example fault geometry (#1) shown in Fig. 6e hosts low total slip, high tortuosity, and lesser overall efficiency. In contrast, the fault geometry (#2) hosts high total slip, low tortuosity, and greater efficiency. The most efficient geometries are those that host the most total fault slip (e.g., Figs. 6, 7). Greater fault slip increases overall efficiency because it reduces the magnitude of off-fault deformation (i.e., internal work), which reduces the normal compression acting on the backwall, and thus the W_{ext}.

6. Discussion

Here we discuss our new insights into the depth of thrust fault initiation, and the relative temporal evolution of thrust fault development in the protothrust zone of accretionary wedges.

6.1. Thrust fault initiation location

Our systematic testing of fault development from varying depths

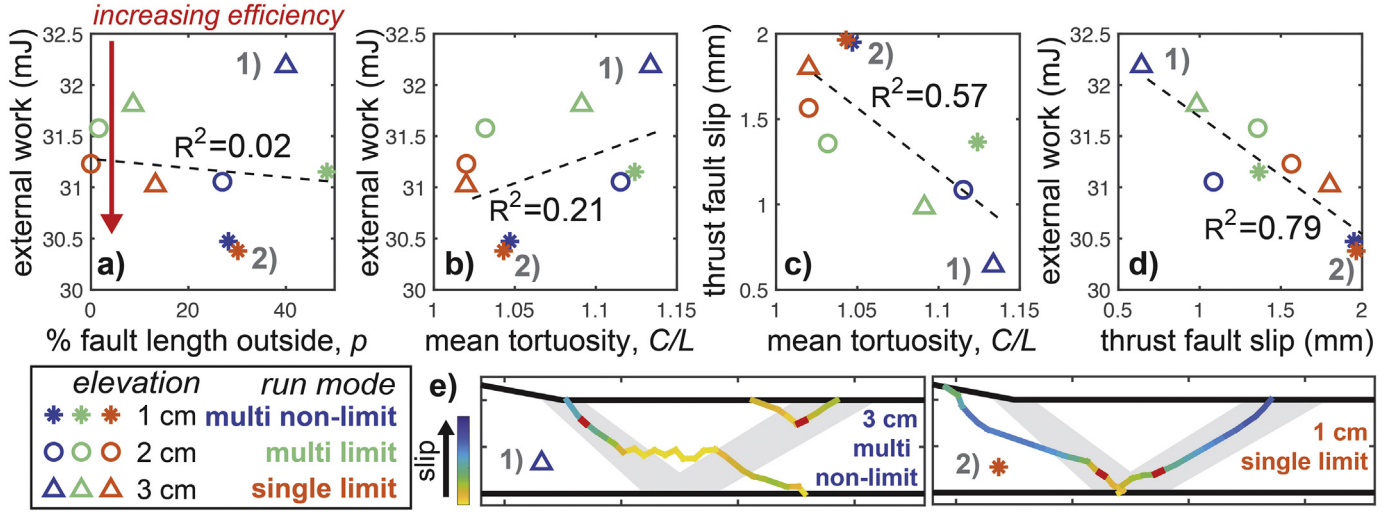

Fig. 6. Comparing efficiency to a) differences in the position of the observed and numerical fault geometries, b) to thrust fault tortuosity, c) to thrust fault slip, and d) comparing tortuosity to thrust fault slip (c). Fault geometries shown in (e) are highlighted with gray numbers in a)-d). The external work of each system is calculated under 0.4 mm applied backwall displacement, and using the final thrust fault geometry propagated in GROW. Faults with higher tortuosity differ more from the observed planar faults with $C/L = 1$. e) The fault geometry shown in model (1), and highlighted in (a-d), hosts low total slip, high tortuosity, and high external work (i.e., lesser efficiency). In contrast, the fault geometry shown in model (2), and highlighted in (a-d), hosts high total slip, low tortuosity, and low external work (i.e., greater efficiency).

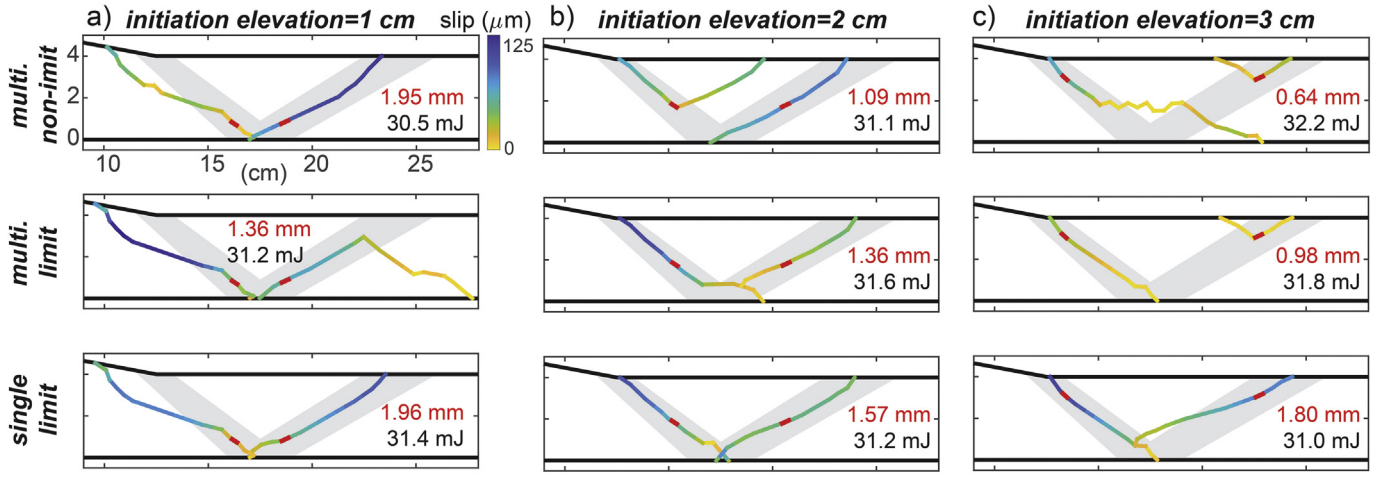

Fig. 7. Predicted fault growth and slip for models with preexisting fractures at 1 cm (a), 2 cm (b) and 3 cm (c) above the detachment, and three run modes: *multiple non-limiting* (top), *multiple limiting* (middle), and *single limiting* (bottom). Fault segments colored by slip. Red lines show the preexisting fractures from which the faults grew. Gray areas show extent of fault geometries typically observed in physical experiments. At this stage of development after the faults have propagated to the topography, detachment or the other fault, higher slip tends to develop along the upper portions of the faults. The red and black numbers are the total thrust fault slip and external work of the model, respectively. Models that host higher slip tend to be more efficient, with lower external work (e.g., Fig. 6). The locations along the faults that host the highest slip by the end of the simulation do not tend to match where the faults initiated. (For interpretation of the references to colour in this figure legend, the reader is referred to the web version of this article.)

suggest that thrust faults initiate at shallow to mid-heights above the detachment, within 50% of the vertical distance to the surface (Fig. 4). Models with faults that initiate at shallow to mid-heights produce fault geometries that more closely match the observed fault geometries than models with faults that initiate at deeper depths. Moreover, models with shallower fractures begin to propagate at lower applied displacements, suggesting the preference for fault initiation at shallower depths.

The applicability of the results of these models to laboratory and crustal accretionary wedges depends on the nature of strain localization leading to macroscopic fault propagation in laboratory and crustal wedges, and the similarity of these processes to the GROW models. Previous analog experiments with the temporal resolution required to observe the fault initiation process suggest that in the initial stages of localization and growth, proto-thrust faults have sub-planar geometries aligned along the orientation and vergence of the eventual system spanning fault (e.g., Dotare et al., 2016; Marshak et al., 2019). These proto-thrust fault geometries agree with the model conceptualization of the proto-thrust geometries included in the models: one element with a length of about 10% of the sandpack height oriented at the dip of the observed through-going faults.

In part due to the careful design of the initial fracture geometry, and its match with the experimental observations, the resulting fracture geometries agree with observations of the shear strain field captured in dry sand accretion experiments (Marshak et al., 2019). These experiments show maximum shear strain within the midpack, and lower shear strain toward the basal detachment and surface of the wedge. This distribution suggests that the forethrust nucleates in the midpack, and then propagates bilaterally both upward and downdip (Marshak et al., 2019), assuming that higher shear strain indicates nucleation location.

Finite-difference numerical models of fault growth within accretionary prisms also produce fault development consistent with our numerical results. Weiss et al. (2018) use a finite difference code to model accretionary fault development. In these models, thrust faults initiate near the topography when the pore pressure is moderate or lower, and near the detachment when the pore pressure is higher. However, in the models of Weiss et al. (2018), backthrusts appear to develop at the slope break and propagate downward even in models with higher fluid pressure (Fig. 7 in Weiss et al., 2018). In our models, fractures near the slope break also propagate downward after linking with the topography and form backthrusts (Figs. 4, 8).

The preference of backthrusts to develop within the upper portion of the sandpack, and then propagate downward in both our models and those of Weiss et al. (2018) likely arises from the higher strain energy density and shear stress that develops near the break in slope between the proto-wedge and flat sandpack, and the reduced compression near the surface (Fig. 3). The reduced compression near the surface allows fractures to fail at lower applied backwall displacement than fractures at deeper depths (e.g., Fig. 5). The higher shear stress and strain energy density near the inflection of the wedge surface promote shallow backthrust development instead of shallow forethrust development because the initial orientation of the backthrust-oriented fracture induces this fracture to propagate with a backthrust-vergence in order to reach this higher shear stress and strain energy density region. Although the shear stress and strain energy density are high near the surface inflection and the bottom left corner of the model, the compressive stress is lower and the Coulomb stress is higher near the surface than near the base (Fig. 3). The overlap of the regions of higher shear stress, higher strain energy density, higher Coulomb stress and lower compression drive upward propagation of the backthrust. The observed preference of faults to propagate into regions with higher strain energy density suggests that the GROW *single* run mode produces fault development consistent with previous work that successfully predicts fault growth using strain energy density (e.g., Du and Aydin, 1993; Okubo and Schultz, 2005; Olson and Cooke, 2005; Fattaruso et al., 2016).

In crustal accretionary prisms, stress concentrations that promote fault growth may develop within smaller volumes and with lower magnitudes than observed in our models. Crustal wedges tend to have smoother transitions in topography (bathymetry) between the more lithified older prism section and the younger frontal protothrust zone than the modeled protowedge and sandpack. Smoother slope transitions may produce lower magnitude shear stress concentrations than the concentrations that develop in the experimental and numerical accretionary wedges. However, mechanical heterogeneities within crustal wedges between the older, more lithified and younger, less lithified portions of the wedge (e.g., Saffer and Tobin, 2011) may also produce stress concentrations that promote fracture initiation.

6.2. Relative temporal evolution of thrust fault development

The newly implemented GROW run modes that only consider

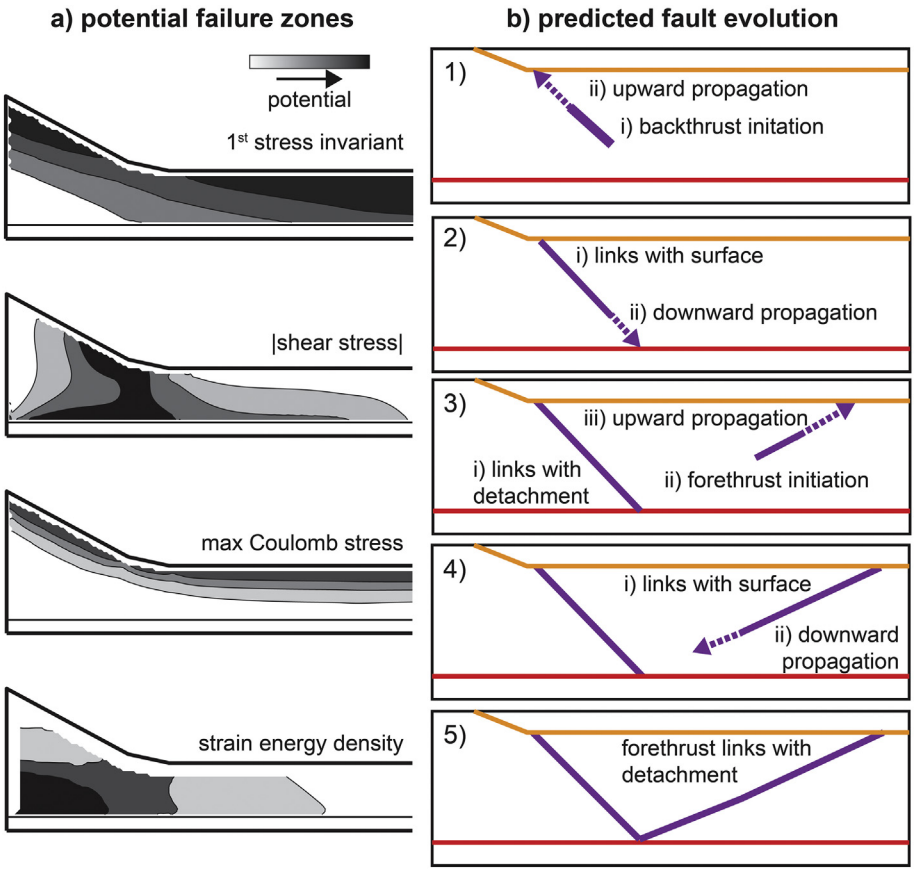

Fig. 8. Schematic representation of potential failure zones (a) and fault growth observed in models (b). a) The stress and strain fields of the models preceding fault development provide broad estimates of the expected zone of fault initiation, shown with darker shades of black. b) The work optimization approach implemented in GROW predicts that first the backthrust initiates and grows upward (1), and then downward (2). Then the backthrust links with the detachment, and the forethrust begins to grow upward (3). Next the forethrust links with the surface and next grows downward (4). Finally, the forethrust links with the detachment and/or backthrust root (5). The backthrust may propagate before the forethrust and upward because of the lower compression, higher magnitudes of shear stress, higher Coulomb stress, and higher strain energy density near the wedge surface slope inflection.

growth from fault tips with the highest stress intensity factors provide detailed insights into the fine-scale temporal development of thrust faults. Moreover, these run modes produce fault geometries that better match the observed fault geometries than the mode that permits all fractures to propagate simultaneously. The limited growth models that include fault initiation in the mid-pack or shallower best match the observed geometries, and show similar relative temporal evolutions of thrust fault development. First, the backthrust initiates, grows upward, and links with the surface (Fig. 8). Then the backthrust propagates downward and links with the detachment, forming a through-going fault. Next the forethrust propagates upward and links with the surface. Then the forethrust propagates downward and links with the detachment, forming a thrust-pair with the backthrust.

The success of the *limiting* run mode to approximate the experimental fault network may reflect the relatively slow loading rate of the accretionary wedge experiments. With faster loading rates, multiple fractures may propagate simultaneously, forming relatively homogenous and isotropic networks (e.g., Fondriest et al., 2017). Under slower loading rates, one or a few fractures may begin to propagate at faster rates, while other fractures arrest their propagation (e.g., Fondriest et al., 2017). In systems with faster loading rates, the *multiple non-limiting* run mode may produce the most accurate fracture geometries.

Previous numerical analyses with planar accretionary thrust faults suggest that the propagation of and subsequent slip along the backthrust produces a greater gain in efficiency relative to newly propagated fault area, $\Delta W_{ext}/\Delta A$, than the forethrust (McBeck et al., 2017a). A planar backthrust produces 20% greater $\Delta W_{ext}/\Delta A$ than a planar forethrust in numerical models based on scaled physical experiments (McBeck et al., 2017a). Collectively, this previous modeling with planar faults and our new contribution with propagating faults suggests that at the onset of thrust faulting, backthrust development produces greater gains in efficiency and consequently initiates before the forethrust. The new models suggest that when the backthrust spans from the surface to the detachment, it impacts the nearby stress field that determines where the forethrust develops. Later, when the forethrust spans from the detachment to the surface, forming a thrust-pair with the backthrust, the forethrust produces larger gains in efficiency relative to the backthrust because it accommodates greater slip (McBeck et al., 2017a).

Del Castello and Cooke (2007) also recognized that planar forethrusts produce greater increases in the total system efficiency than backthrusts when these faults span from the basal detachment to the surface. In that set of models, the steeper dips of backthrusts relative to forethrusts, designed from experimental observations of Adam et al. (2004), cause them to accommodate less horizontal contraction than forethrusts, which then leads to greater internal work done within the wedge (Del Castello and Cooke, 2007). Backthrusts may accommodate slip for less time than forethrusts in scaled physical accretionary experiments (Mulugeta and Koyi, 1992) because of their lesser ability to accommodate contraction along their steeper dips (Del Castello and Cooke, 2007). The backthrusts in our physical experiments and models with planar through-going faults host steeper dips than the forethrusts, consistent with the steeper backthrust dips observed in previous work.

Although shear strain fields captured throughout physical accretion experiments lack the temporal resolution to distinguish the relative timing of thrust development, they show greater localized shear strain along the forethrust than the backthrust at the onset of localization (Dotare et al., 2016; McBeck et al., 2017a, 2018; Marshak et al., 2019). Similar to the shear strain distribution, the horizontal normal strain reveals more localized contraction along the forethrust than the backthrust (McBeck et al., 2018). However, the vertical extension shows a similar degree of localization along the backthrust and forethrust at this stage (McBeck et al., 2018). The localized vertical extension along the early backthrust suggests that this fault is effective at accommodating thickening of the sandbox early in the experiment.

Shear strain fields captured at higher temporal resolution are

consistent with the shallow nucleation and downward propagation of backthrusts observed in the GROW models (Dotare et al., 2016). The observed backthrusts in these experiments tend to host higher shear strain near the surface than at depth near the root of the forethrust, suggesting initiation near the surface (Fig. 6 in Dotare et al., 2016). In contrast to the models presented here, time series of shear strain fields of some scaled accretionary wedges led previous workers to suggest that the forethrust develops into a through-going fault before the backthrust (Dotare et al., 2016; Marshak et al., 2019). These observations may arise because higher shear strain develops along the forethrust than the backthrust in accretion experiments. However, the models of the present study demonstrate that through-going thrust faults may have the greatest slip at depths where they did not initiate (Fig. 7). For example, when the faults initiate at the deepest depth, 1 cm above the detachment and in the *single limiting* run mode, at the end of the simulation when the faults intersect both the surface and detachment fault, they host the largest slip near the wedge surface. Consequently, patterns of strain along young through-going thrust faults may not reliably indicate the propagation history.

7. Conclusions

Our results shed light on the ability of work optimization to predict the spatial development and temporal sequence of thrust fault networks at the frontal toe of accretionary systems. These results suggest that work optimization provides a robust method of predicting the spatial development of fault networks, consistent with previous analyses (Del Castello and Cooke, 2007; Cooke and Madden, 2014; McBeck et al., 2016; McBeck et al., 2017a, 2017b; Madden et al., 2017). The findings of this contribution provide novel insights on the potential depth of thrust fault initiation, thrust propagation direction, and relative timing of thrust fault development within the proto-thrust region of accretionary wedges. The degree of propagation synchronicity between multiple faults, which may reflect the relative loading rate, impacts the details, but not the first-order thrust fault geometry. The work optimization approach implemented in GROW predicts that accretionary thrust faults initiate in the mid-pack and shallower depths, rather than adjacent to the detachment fault. This optimization approach predicts that backthrusts propagate before forethrusts, and that thrusts tend to propagate upward first, and then downward. GROW predicts thrust fault development with greater success when only the most efficient fault grows at each time increment, rather than all of the faults. The model results show that the final slip distributions do not reliably indicate the initiation location of the faults.

Supplementary data to this article can be found online at https://doi.org/10.1016/j.tecto.2020.228461.

Declaration of Competing Interest

The authors declare that they have no known competing financial interests or personal relationships that could have appeared to influence the work reported in this paper.

Acknowledgements

This work was supported in part by a Geological Society of America Student Research Grant and an International Association of Mathematical Geologists Student Research Grant to JM, and NSF grant EAR-1650368 to MC. The modeling code GROW and input files are available on GitHub (https://github.com/jmcbeck/Numerical_fault_growth_accretion). Reviews by Editor Agard and three anonymous reviewers helped improve this manuscript.

References

Adam, J., Klaeschen, D., Kukowski, N., Flueh, E., 2004. Upward delamination of Cascadia Basin sediment infill with landward frontal accretion thrusting caused by rapid glacial age material flux. Tectonics 23 (3). https://doi.org/10.1029/2002TC001475.

Barnes, P.M., Ghisetti, F.C., Ellis, S., Morgan, J.K., 2018. The role of protothrusts in frontal accretion and accommodation of plate convergence, Hikurangi subduction margin, New Zealand. Geosphere 14 (2), 440–468.

Baud, P., Zhu, W., Wong, T.F., 2000. Failure mode and weakening effect of water on sandstone. J. Geophys. Res. Solid Earth 105 (B7), 16371–16389.

Baud, P., Wong, T.F., Zhu, W., 2014. Effects of porosity and crack density on the compressive strength of rocks. Int. J. Rock Mech. Min. Sci. 67, 202–211.

Booth-Rea, G., Klaeschen, D., Grevemeyer, I., Reston, T., 2008. Heterogeneous deformation in the Cascadia convergent margin and its relation to thermal gradient (Washington, NW USA). Tectonics 27 (4).

Buiter, S.J., Schreurs, G., Albertz, M., Gerya, T.V., Kaus, B., Landry, W., le Pourhiet, L., Mishin, Y., Egholm, D., Cooke, M., Maillot, B., Thieulot, C., Crook, T., May, D., Souloumiac, P., Beaumont, C., 2016. Benchmarking numerical models of brittle thrust wedges. J. Struct. Geol. 92, 140–177.

Cooke, M.L., Madden, E.H., 2014. Is the Earth lazy? A review of work minimization in fault evolution. J. Struct. Geol. 66, 334–346. https://doi.org/10.1016/j.jsg. 2014.05.004.

Cooke, M.L., Pollard, D.D., 1997. Bedding plane slip in initial stages of fault-related folding. J. Struct. Geol. 19, 567–581.

Del Castello, M., Cooke, M.L., 2007. Underthrusting-accretion cycle: work budget as revealed by the boundary element method. J. Geophys. Res. 113 (B12404), 1–14. https://doi.org/10.1029/2007JB004997.

Dempsey, D., Ellis, S., Archer, R., Rowland, J., 2012. Energetics of normal earthquakes on dip-slip faults. Geology 40 (3), 279–282.

Dotare, T., Yamada, Y., Adam, J., Hori, T., Sakaguchi, H., 2016. Initiation of a thrust fault revealed by analog experiments. Tectonophysics. https://doi.org/10.1016/j.tecto.2015.12.023.

Du, Y., Aydin, A., 1993. The maximum distortional strain energy density criterion for shear fracture propagation with applications to the growth paths of enechelon faults. Geophys. Res. Lett. 20 (11), 1091–1094.

Fattaruso, L.A., Cooke, M.L., Dorsey, R.J., Housen, B.A., 2016. Response of deformation patterns to reorganization of the southern San Andreas fault system since ca. 1.5 Ma. Tectonophysics 693, 474–488.

Fondriest, M., Doan, M.L., Aben, F., Fusseis, F., Mitchell, T.M., Voorn, M., Secco, M., Di Toro, G., 2017. Static versus dynamic fracturing in shallow carbonate fault zones. Earth Planet. Sci. Lett. 461, 8–19.

Gercek, H., 2007. Poisson's ratio values for rocks. Int. J. Rock Mech. Min. Sci. 44 (1), 1–13.

Hardy, S., Duncan, C., Masek, J., Brown, D., 1998. Minimum work, fault activity and the growth of critical wedges in fold and thrust belts. Basin Res. 10, 365–373. https://doi.org/10.1046/j.1365-2117.1998.00073.x.

Klinkmüller, M., Schreurs, G., Rosenau, M., Kemnitz, H., 2016. Properties of granular analogue model materials: a community wide survey. Tectonophysics 684, 23–38.

Lohrmann, J., Kukowski, N., Adam, J., Oncken, O., 2003. The impact of analogue material properties on the geometry, kinematics, and dynamics of convergent sand wedges. J. Struct. Geol. 25 (10), 1691–1711.

Madden, E.H., Cooke, M.L., McBeck, J., 2017. Energy budget and propagation of faults via shearing and opening using work optimization. J. Geophys. Res. Solid Earth 122 (8), 6757–6772.

Marshak, S., Haq, S.S., Sen, P., 2019. Ramp initiation in fold-thrust belts: Insight from PIV analysis of sandbox models. J. Struct. Geol. 118, 308–323.

Masek, J.G., Duncan, C., 1998. Minimum-work mountain building. J. Geophys. Res. Solid Earth 103 (B1), 907–917.

McBeck, J., Madden, E., Cooke, M., 2016. Growth by Optimization of Work (GROW): a new modeling tool that predicts fault growth through work minimization. Comput. Geosci. 88, 142–151.

McBeck, J., Cooke, M.L., Herbert, J.W., Maillot, B., Souloumiac, P., 2017a. Work optimization predicts accretionary faulting: an integration of physical and numerical experiments. J. Geophys. Res. Solid Earth 122 (9), 7485–7505.

McBeck, J., Cooke, M., Madden, E., 2017b. Work optimization predicts the evolution of extensional step overs within anisotropic host rock: Implications for the San Pablo Bay, CA. Tectonics 36 (11), 2630–2646.

McBeck, J., Cooke, M.L., Souloumiac, P., Maillot, B., Mary, B., 2018. The influence of detachment strength on the evolving deformational energy budget of physical accretionary prisms. Solid Earth 9, 1421–1436. https://doi.org/10.5194/se-9-1421-2018.

Mulugeta, G., Koyi, H., 1992. Episodic accretion and strain partitioning in a model sand wedge. Tectonophysics 202 (2), 319–333.

Okubo, C.H., Schultz, R.A., 2005. Evolution of damage zone geometry and intensity in porous sandstone: insight gained from strain energy density. J. Geol. Soc. 162 (6), 939–949.

Olive, J.A., Behn, M.D., 2014. Rapid rotation of normal faults due to flexural stresses: an explanation for the global distribution of normal fault dips. J. Geophys. Res. Solid Earth 119 (4), 3722–3739.

Olson, E.L., Cooke, M.L., 2005. Application of three fault growth criteria to the Puente Hills thrust system, Los Angeles, California, USA. J. Struct. Geol. 27 (10), 1765–1777.

Reches, Z.E., Lockner, D.A., 1994. Nucleation and growth of faults in brittle rocks. J. Geophys. Res. Solid Earth 99 (B9), 18159–18173.

Saffer, D.M., Tobin, H.J., 2011. Hydrogeology and mechanics of subduction zone forearcs: Fluid flow and pore pressure. Annu. Rev. Earth Planet. Sci. 39, 157–186. https://doi.

org/10.1146/annurev-earth-040610-133408.
Schreurs, G., Buiter, S.J., Boutelier, J., Burberry, C., Callot, J.P., Cavozzi, C., Cerca, M., Chen, J.H., Cristallini, E., Cruden, A.R., Cruz, L., 2016. Benchmarking analogue models of brittle thrust wedges. J. Struct. Geol. 92, 116–139.
Tang, C.A., Lin, P., Wong, R.H.C., Chau, K.T., 2001. Analysis of crack coalescence in rock-like materials containing three flaws—part II: numerical approach. Int. J. Rock Mech. Min. Sci. 38 (7), 925–939.
Weiss, J.R., Ito, G., Brooks, B.A., Olive, J.A., Moore, G.F., Foster, J.H., 2018. Formation of the frontal thrust zone of accretionary wedges. Earth Planet. Sci. Lett. 495, 87–100.
Yagupsky, D.L., Brooks, B., Whipple, K., Duncan, C., Bevis, M., 2014. Distribution of active faulting along orogenic wedges: minimum-work models and natural analogue. J. Struct. Geol. 66, 90–101. https://doi.org/10.1016/j.jsg.2014.05.025.